Studies on poly(vinylidene fluoride)–clay nanocomposites: Effect of different clay modifiers

T. Umasankar Patro, Milind V. Mhalgi, D.V. Khakhar*, Ashok Misra

Department of Chemical Engineering, Indian Institute of Technology Bombay, Powai, Mumbai 400076, India

Keywords:
Organoclay
PVDF
Nanocomposites

A B S T R A C T

Montmorillonite clay based poly(vinylidene fluoride) nanocomposites were prepared by melt-mixing. The clays used included unmodified clay, a commercially available ammonium based clay, and two organically modified clays prepared by cation exchange with hexadecylpyridinium chloride and with octadecyltriphenylphosphonium bromide. PVDF–clay nanocomposites were processed in a mini twin-screw extruder. The structure of nanocomposites, analyzed using WAXD and TEM, indicated different extents of the clay dispersion depending on the modifier. PVDF formed β-phase crystals in the presence of organically modified clay when crystallized from its melt; in contrast, α-crystals were formed in the absence of clay and with unmodified clay. SAXS analysis indicated that the long period and crystalline lamella thickness decreased with the addition of clay. The melting and crystallization temperatures increased around 10 and 13 °C, respectively, with 5 wt% of phosphonium modified clay, which was the highest among the clays used. Further, the clay served as a nucleating agent for PVDF matrix, as observed by hot-stage polarized optical microscopy. The average spherulitic radius, determined from small angle light scattering, decreased with clay content. The elongation at break increased around 200% with the addition of only 5 wt% of ammonium clay. The storage and loss moduli of the nanocomposites were significantly higher than those of PVDF throughout the temperature range. Dielectric measurements showed a maximum increase of about 8 units of dielectric constant at 1 Hz frequency with 5 wt% organoclay.

1. Introduction

Poly(vinylidene fluoride) (PVDF) is a semi-crystalline polymer and has four crystal polymorphs referred to as α, β, γ and δ [1,2]. The α and β polymorphs are most common, but melt processing usually results in the α-phase. The β-phase has an all-*trans* conformation comprising fluorine atoms and hydrogen atoms on opposite sides of the polymer backbone, resulting in a net non-zero dipole moment [1]. Consequently, this phase exhibits good electrical properties such as a high piezoelectric constant [3,4] and dielectric constant [4]. The β-phase in PVDF can be obtained from the α-phase by uniaxial or biaxial stretching of PVDF film [6,7] and simultaneous stretching and poling of the film. Other methods for obtaining β-phase have also been proposed [5,8,9]. PVDF is used for pipes and fittings in chemical processing and pharmaceutical industries due to its inertness. In its β-phase, PVDF is also used in polymer sensors, actuators and transducers. The blending of organically modified clay with PVDF affects both mechanical and electrical properties and we review some of the previous studies below.

Priya and Jog [10–12] were the first to prepare PVDF–clay nanocomposites. They observed that the addition of organically modified clay resulted in the formation of the β-phase instead of the α-phase upon melt processing. They used two different organoclays (Cloisite® 6A and Cloisite® 20A) in separate studies. Nanocomposites prepared with both the clays (1.5–7 wt%) showed an increase in melting (6–8 °C) and crystallization (10–12 °C) temperatures, crystallization rate and a decrease in the crystallinity (about 17%). The storage modulus was found to be increased significantly with clay [10–12]. Shah et al. [13] found a significant enhancement in toughness (~700%) (defined by the area under the stress–strain curve) of PVDF on the addition of only 5 wt% of organoclay (Cloisite® 30B). Young's modulus and elongation at break of nanocomposites were reported to be around 40 and 250% higher than those of the PVDF matrix, respectively. They also reported that PVDF with pristine and surface-modified silica as well as with unmodified layered silicate all had similar toughness. As observed by Priya and Jog [10], they also found a complete phase transformation of the PVDF to its β-phase on the addition of 2 wt% organoclay. It was suggested that the matching of crystal lattice of the clay with that of the β-phase of PVDF is probably responsible for the formation and stabilization of the β-phase. They argued that in the case of nanocomposites the structure formed by the

nucleation of fiber-like β-phase on the clay surface is suitable for plastic flow under applied stress, leading to increase in the toughness of the material. The recent SAXS studies by Shah et al. [14] show that the silicate layers gain the ability to orient in the direction of applied stress and become more mobile in polymer matrix when the measurement is carried out above the glass transition temperature of the polymer. Thus the nanoparticle orientation and alignment under tensile stress are responsible for the energy dissipation and ultimately increase in the toughness of PVDF nanocomposites. They observed that the toughness of the nanocomposites decreased at higher clay percentages (>5 wt%) and at lower temperature (−65 °C for 5 wt% of clay loading) [14]. Molecular dynamics simulations on nanoparticle mobility in a polymer matrix have also suggested that the increase in toughness results from the ability of nanoparticles to dissipate energy due to the equivalence of the time scales of motion of the particles and the polymer molecules [15].

Dillon et al. [16] prepared PVDF–clay nanocomposites using Cloisite® 15A and Cloisite® 25A by two methods: solution casting and co-precipitation. The nanocomposites prepared by solution casting were phase separated (microcomposites) with Cloisite® 15A and partially intercalated structure with Cloisite® 25A clay. However, the nanocomposites prepared by co-precipitation gave complete exfoliation of the clay layers. The crystallization behaviour of nanocomposites was in agreement with that reported by Priya and Jog [11]. Buckley et al. [17] studied the impact of cold crystallization on the structure of PVDF-organically modified clay (Lucentite STN™) nanocomposites. It was observed that the nanocomposites having organically modified clay in the range of 0.025–0.5 wt% partially formed β-phase, however, with 0.5 wt% or more of organoclay the β-phase dominated in PVDF. The nanocomposites with a predominant β-phase showed a broader SAXS peak than the samples having α-phase [17]. A study of rheological behaviour of clay based PVDF–PMMA miscible blend nanocomposites [18] showed that at lower frequencies, the storage modulus increased with PMMA content in nanocomposites and at 10% PMMA, the frequency dependency of the storage modulus showed solid-like behaviour. Paraelectric and ferroelectric phase transitions were observed by Cebe and Runt [19] by adding organically modified layered silicates (Nanomer 1.30TC and Lucentite STN) in poly(vinylidene fluoride-*co*-trifluoroethylene). It was found that the nanocomposites with 2 wt% organoclay showed a crystal nucleating effect and an increase in the number of ferroelectric crystals formed during cooling from melt. At higher clay loading (10–25 wt%), the temperature stability range of the ferroelectric crystals increased significantly [19].

The present work primarily concerns the preparation of PVDF–clay nanocomposites using unmodified and different organically modified clays by the melt-mixing method. The modifiers used are C_{18} and C_{16} chains of phosphonium and pyridinium salts, respectively, and dimethylbenzylhydrogenated tallow quaternary ammonium. Clays with ammonium based modifier have been used extensively in PVDF nanocomposites in previous studies [10–14,16,17], but the behaviour of nanocomposites with phosphonium and pyridinium based clays has not been previously studied. Phosphonium and pyridinium based clays are known to have greater thermal stability compared to ammonium based clays [20,21]. Nanocomposites with 0.5–5 wt% of different clays are prepared through melt-mixing method. The purpose of the present study is to investigate the effect of different clay modifiers on the structure, crystallization behaviour, and mechanical and electrical properties of PVDF–clay nanocomposites.

2. Experimental details

2.1. Synthesis of octadecyltriphenylphosphonium bromide

The method for synthesizing the above compound was similar to the method adopted by Zhu et al. [20]. The reaction scheme is presented in Fig. 1. The required amount of triphenylphosphine (1 M) (Otto Kemi, India) and 1-bromo octadecane (1.2 M) (Spectrochem, India) was placed in a 250 ml round bottomed flask. The reaction was carried out by stirring the mixture with a magnetic stirrer at 100 °C for 10 h in nitrogen atmosphere. 1-Bromo octadecane was added slightly in excess to ensure the completion of the reaction; it is easily removed by petroleum ether. The white powder like product was then washed three times with petroleum ether. The yield was found to be 80%. The product was dried for 12 h under vacuum at room temperature. The ^{13}C NMR ($CDCl_3$, δ, ppm) peaks were found to be at 135.0 (d, $J = 2$ Hz, P–C), 133.6 (d, $J = 10$ Hz, P–C), 130.5 (d, $J = 13$ Hz, P–C), 118.3 (d, $J = 85$ Hz, P–C), 31.8, 30.4 (d, $J = 15$ Hz, P–CH_2), 29.3 (m), 23.1, 22.6, 14.0 and the ^{31}P NMR ($CDCl_3$, δ, ppm) was at 22.4, confirming the formation of the product.

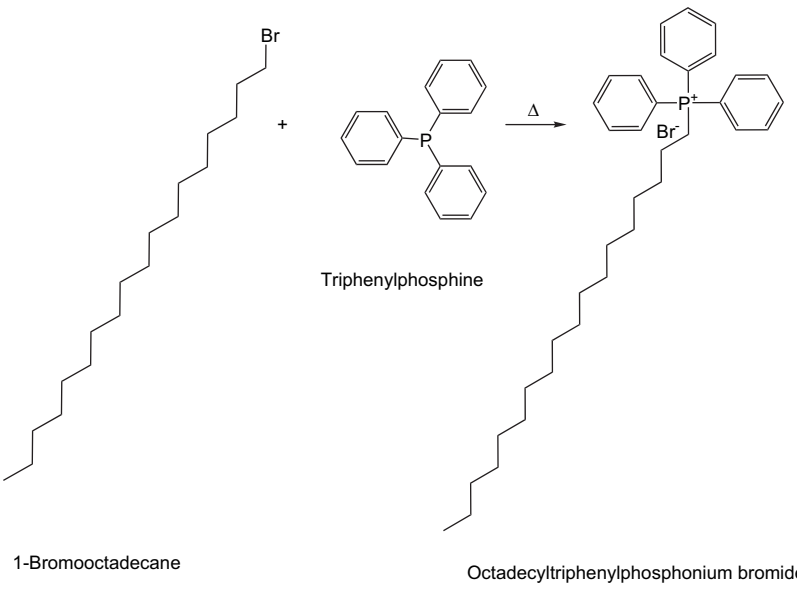

Fig. 1. Scheme for the synthesis of octadecyltriphenylphosphonium bromide.

2.2. Clay modification using different surfactants

Two types of organic surfactants were used to modify the clay, viz., hexadecylpyridinium chloride (Otto Kemi, India) and octadecyltriphenylphosphonium bromide. The method of clay modification for all the surfactants is similar. The clay was modified by using cation exchange reaction. Ten grams of unmodified clay (Cloisite® Na^+, Southern Clay Products, USA) was dispersed in 500 ml of deionized water by using a magnetic stirrer at 60 °C. A fixed amount of surfactants (1.2 meq/1 g of CEC of clay) was dissolved in 50:50 mixture by volume of water and methanol. The solution was then slowly poured into the clay suspension along with stirring. A white precipitate was observed immediately after the transfer of the surfactant solution, indicating the beginning of exchange reaction. The reaction was continued for 12 h to ensure the complete exchange of cations. The precipitate was filtered and washed repeatedly with mixture of water and methanol until no white precipitate of chloride ion with $AgNO_3$ solution was obtained. The clay was vacuum-dried for 24 h at 100 °C. The lumps of clay after drying were ground using a ball-mill to a fine powder.

2.3. Nanocomposite preparation

All clays and PVDF (Kynar 720, Atofina, USA) were dried under vacuum at 100 °C overnight prior to processing. PVDF–clay nanocomposites were prepared with different organoclays by using a mini twin-screw extruder (Micro 5, DSM, Holland) with co-rotating screws and a 5 cc capacity barrel. Various weight percentages, ranging from 0.5 to 5 wt%, of each clay were melt-mixed with PVDF. The processing temperature, residence time and the screw speed were set at 210 °C, 5 min and 100 rpm, respectively. The details of organoclays are given in Table 1.

2.4. X-ray diffraction

Wide angle X-ray diffraction (WAXD) studies were carried out for all the nanocomposite and clay samples by using Cu-K_α radiation for X-ray of wavelength 1.54 Å between 3°–40° and 3°–10° 2θ, respectively, at 0.2°/20 s scan rate in an X-ray diffractometer (X'Pert Pro, PANalytical).

Small angle X-ray scattering (SAXS) experiments were performed on compression-molded polymer films of thickness 80 (±10) μm using an X-ray source having wavelength 1.54 Å in a diffractometer (Anton Paar, Austria). The samples were scanned for 15 min at 25 °C between $2\theta = 0°$ and 8°. The scattering patterns were recorded on a film using the line collimation technique. The scattering patterns were integrated to generate an $I(q)$ vs. q curve, where $I(q)$ is the intensity of scattered X-rays and q is the scattering vector. Lorentz's corrected intensity, $I(q)q^2$, was plotted vs. q for all the samples to determine the long period, L_w, and crystalline lamellar thickness, L_c. The long period was calculated using Bragg's equation, $L_w = 2\pi/q_m$, where q_m is the value of the scattering vector corresponding to the maximum of $I(q)q^2$. The crystalline lamellar thickness was obtained using $L_c = L_w X_c$, where X_c is crystallinity which was measured from DSC traces.

Table 1
Nanocomposite samples used in the study

Sample	Clay type	Modifier	Clay percentages (%) (x)
PVDF	–	–	0
PVDF(x)CNa	CNa	–	2, 5
PVDF(x)C10A	C10A	Dimethylbenzylhydrogenated tallow quaternary ammonium	0.5, 1, 2, 5
PVDF(x)C18P	C18P	Octadecyltriphenylphosphonium bromide	0.5, 1, 2, 5
PVDF(x)CHDP	CHDP	Hexadecylpyridinium chloride	2, 5

2.5. Fourier transform infrared spectroscopy

PVDF film samples were characterized by using FTIR (Nicolet, USA) to determine the crystalline phases that were obtained on the addition of clay. FTIR measurements were made on the compression-molded films of thickness of around 40–50 μm in the wavelength range of 400–4000 cm^{-1} with a resolution of 2 cm^{-1} followed by background correction. The fraction of β-phase in film samples was determined from the FTIR scans as

$$F(\beta) = \frac{A_\beta}{\left(1.3A_\alpha + A_\beta\right)} \quad (1)$$

where A_α and A_β are the absorbances in FTIR spectrum corresponding to 764 and 840 cm^{-1} bands, respectively [22].

2.6. Transmission electron microscopy

TEM (Philips CM 200) was carried out to study the dispersion of clay. Samples for TEM were prepared using an ultra-microtome (Leica, Ultracut UCT). Around 70–100 nm thick films were cut along the flow direction of an injection-molded tensile specimen using a freshly prepared glass knife. The thickness of the films was determined from the given color chart. One of the films was transferred to the TEM copper grid and stained with ruthenium tetroxide for about 10 min before analysis.

2.7. Thermal analysis

Crystallization studies were conducted by means of DSC (Pyris6, Perkin Elmer analyzer). The samples were analyzed between 50 and 200 °C at a heating or cooling rate of 10 °C/min. The samples were kept for 3 min at 200 °C to erase the thermal history. The first cooling and second heating traces were recorded. The percentage crystallinity was calculated using the heat of fusion value for 100% crystalline PVDF, $\Delta H_{100\%} = 102.7$ J/g [23]. Thermogravimetric analysis (High resolution TGA 2950, TA instruments) studies were carried out in an N_2 atmosphere between room temperature and 800 °C at the rate of 20 °C/min.

2.8. Hot-stage polarized optical microscopy

Spherulitic growth was observed by hot-stage optical microscopy (Linkam TP 94 hot-stage mounted on an Olympus optical microscope). The material was rapidly heated up to 200 °C and kept for 5 min at this temperature to ensure the melting of all the crystals. It was then quenched to 156 °C (for pure PVDF), 163 and 170 °C (for nanocomposite samples) at a rate of 50 °C/min and maintained at that temperature until the spherulitic growth ceased. The micrographs were captured with the help of a camera attached to the microscope.

2.9. Small angle light scattering (SALS)

SALS experiments were carried out to determine the spherulitic radius from the four-lobe patterns obtained. A He–Ne laser having wavelength 632.7 Å was used as a light source. The patterns formed on the screen were captured using a digital camera (Nikon, Coolpix, Japan). The spherulitic radius was calculated using [24]

$$R = \frac{1.025\lambda_0}{\pi n \sin(\theta'_m/2)} \quad (2)$$

where R = average spherulitic radius, λ_0 = wavelength of the light in the air, and θ'_m = corrected scattering angle for maximum intensity, which is related to the actual scattering angle, θ_m, as $\sin\theta'_m = \sin(\theta_m)/n$, where $n = 1.42$ is the refractive index of the sample.

2.10. Tensile testing

The samples were injection-molded in a microinjection-molding machine (DSM, Holland) from its melt at 220 °C to make tensile specimens. The mold was kept at room temperature. Tensile testing was conducted on the dumb-bell shaped specimen of 3 mm thickness and width each and 12 mm gauge length (ASTM D638 Type V) using a UTM (Instron 3365) equipped with a 10 kN load cell. The cross-head speed was set at 5 mm/min.

2.11. Dynamic mechanical analysis

Dynamic mechanical analysis was performed in tension mode on compression-molded film samples by using a Dynamic Mechanical Analyzer (Triton, UK). The length, width and thickness of the samples were kept in the range of 2, 3–4 and 0.050–0.060 mm, respectively. The tests were performed in the temperature range between −100 and 150 °C. The samples were heated at a rate of 2 °C/min. The frequency of tension was set at 1 Hz and the deflection was 0.02 mm.

2.12. Dielectric constant measurements

Dielectric measurements were performed on compression-molded disc-shaped films of thickness 80–90 μm and diameter 20 mm. The samples were silver-coated on opposite faces and the measurements were carried out between frequencies 1 Hz and 1 MHz in a high-resolution dielectric analyzer (Novocontrol, Germany). The dielectric constant (ε_r) of samples was determined by using $C = \varepsilon_r\varepsilon_o(A/d)$, where C = capacitance, $\varepsilon_o = 8.85 \times 10^{-12}$ F m^{-1} is permittivity of vacuum, A is the area of the electrode and d is the thickness of the sample.

3. Results and discussion

3.1. Thermogravimetric analysis of clay

The curves for mass loss vs. temperature are plotted in Fig. 2. It can be seen that in the case of unmodified clay the initial mass loss of about 6% between room temperature and 150 °C is due to the evaporation of moisture present in the clay. However, upon modification of the clay, the organoclays do not show significant mass loss up to the temperature 200 °C. The maximum mass loss of about 0.8% is observed up to 200 °C in the case of pyridinium clay (CHDP), whereas the phosphonium modified clay (C18P) shows about 0.2% mass loss in the above temperature range. This indicates the hydrophobic nature of clay in presence of phosphonium surfactants. The parameters determined from thermogravimetric analysis are presented in Table 2. The onset of decomposition temperature is found to be in the order of phosphonium (C18P) (301 °C) > pyridinium (CHDP) (248 °C) > ammonium clay (C10A) (177 °C) (Table 2), indicating a greater thermal stability of phosphonium clay compared to other clays. Organic content is higher in the case of ammonium clay (36.7%) than phosphonium (28.2%) and pyridinium clays (26.1%). The phosphonium and pyridinium clays prepared using cation exchange reaction show lower values of organic contents than the theoretically calculated values using CEC of montmorillonite clay (92.6 meq/100 g). This indicates that the surfactant molecules weakly bonded to the surface of the clay are removed by the deionized water used for repeated washings of the clay after modification.

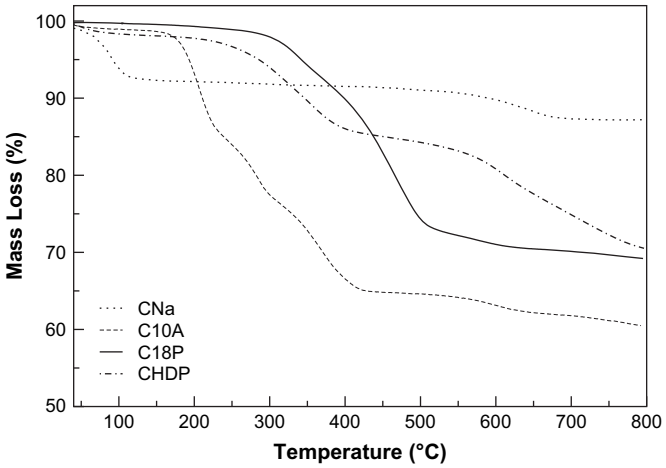

Fig. 2. TGA of unmodified clay and organoclays.

3.2. Clay dispersion

Fig. 3 presents the WAXD patterns of PVDF nanocomposites with unmodified clay (Fig. 3a) and modified clays (Fig. 3b–d). The unmodified clay has a d-spacing of 12.1 Å, the XRD peak for which is seen at $2\theta \sim 7°$. In the nanocomposites with unmodified clay (Fig. 3a), the clay peak is shifted towards the left, resulting in a diffused peak at $2\theta \sim 5.5°$, corresponding to d-spacing of 15.1 Å for both the clay percentages (2 and 5 wt%). This suggests that the unmodified clay forms an intercalated nanocomposite structure, even without any organic modifier. This type of structure is formed due to the interaction between the unmodified clay and PVDF or because of shear induced intercalation. The absence of the $d_{(001)}$ peak in the case of PVDF with modified clays, C10A and CHDP indicates the formation of exfoliated nanocomposites (Fig. 3(b) and (d)). The peak at $2\theta \sim 6°$ in Fig. 3(b) corresponding to the d-spacing 14.5 Å, which is seen in all the C10A nanocomposite samples, could be a resultant peak of second order diffraction, i.e., $d_{(002)}$ [25]. The peak is due to a partially collapsed structure resulting from quaternary ammonium degradation [26], as the processing temperature (210 °C) of polymer is higher than the onset temperature of decomposition (177 °C) for C10A. However, the second order peak is not obtained with other organoclays (C18P and CHDP), which might be due to the higher onset temperature of decomposition shown by these clays (Table 2) and hence they are stable at the processing temperature. WAXD patterns of PVDF with C18P nanocomposites did not show any shifting of the $d_{(001)}$ peak (Fig. 3(c)). However, the relative intensity of the peak reduced significantly at lower percentages of clay loading. This suggests that the clay is exfoliated but a small fraction of the clay remains as local aggregates in C18P nanocomposites.

TEM images for nanocomposites are shown in Fig. 4. Bright field TEM images for 2 wt% of C10A, C18P and CHDP (Fig. 4(a)–(d)) show clay tactoids aligned in the flow direction (the black lines represent the clay layers). It can be seen that the clay tactoids are dispersed uniformly into the PVDF matrix. The thickness and length of the clay tactoids are found to be in the range of 5–60 and 100–600 nm, respectively. However, there are some individual clay layers

Table 2
Parameters obtained from TGA of clay

Clay	Moisture content (%)	Onset of decomposition, T_{onset} (°C)	Organic content (%)
CNa	6.0	–	0
C10A	0.5	177	36.7
C18P	0.2	301	28.2
CHDP	0.8	248	26.1

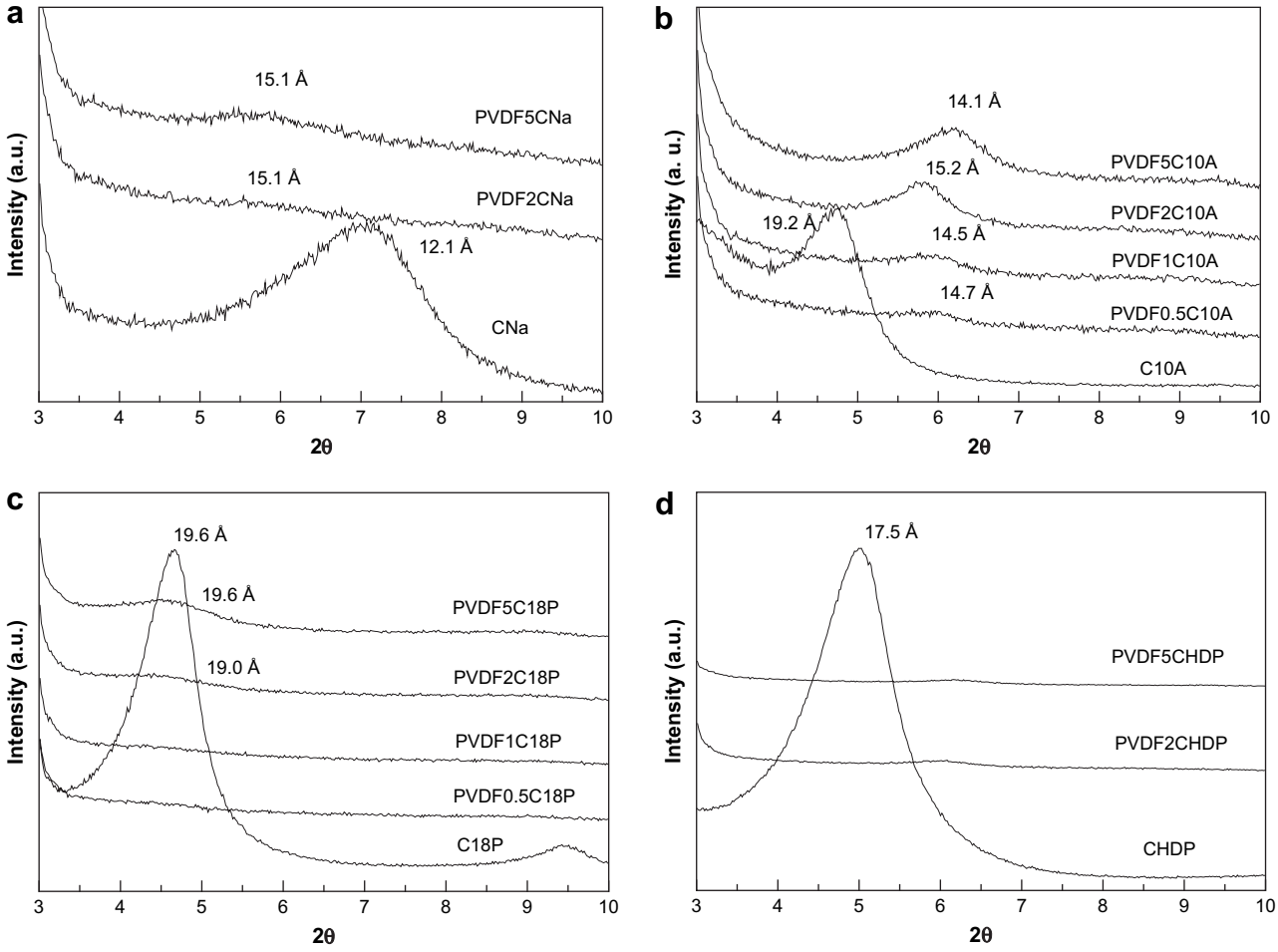

Fig. 3. WAXD of PVDF with (a) CNa, (b) C10A, (c) C18P and (d) CHDP nanocomposites.

separated from the tactoids as shown in Fig. 4. This indicates a very good dispersion or exfoliation of clay layers in the polymer matrix. The average thicknesses of tactoids are measured using image analysis software (ImagePro Plus) and are given in Table 3. Nanocomposites prepared using C10A and CHDP clays show better exfoliation of clay tactoids than C18P. The average thickness of the silicate layers was found to be around 1.1 nm. This is in agreement with the reported value [27].

3.3. Phase behaviour

The α-phase peaks of pure PVDF in WAXD (Fig. 4) observed at $2\theta \approx 17.5°, 18.2°$ and 19.7° correspond to the (100), (020) and (110) planes and *d*-spacings of 5.06, 4.86 and 4.50 Å, respectively. Fig. 5(a) presents the WAXD patterns of PVDF with unmodified clay. It is clear from the figure that the addition of unmodified clay does not alter the crystalline peaks much, showing predominantly α-phase in spite of forming an intercalated nanocomposite structure. In the composites with 2 wt% unmodified clay (Fig. 5(a)), the (110) α-peak is shifted slightly towards the right approaching the β-phase peak, which indicates the formation of some β-PVDF. The small shoulder peak at $2\theta \approx 26.3°$, which is the characteristic peak of α-phase in pure PVDF [28], corresponding to (201) and (310) planes becomes prominent on the addition of unmodified clay. Figs. 5(b) and 6(a) and (b) present the WAXD of PVDF nanocomposites with C10A, CHDP and C18P, respectively. On the addition of the above organoclays, the α-PVDF peaks disappear and a new peak is observed at $2\theta \sim 20.3°$, for all clay percentages and modifiers. This is a composite peak of (110) and (200) planes of β-PVDF [28–31].

The formation of β-phase is again confirmed by the absorption peaks in FTIR spectra (Figs. 7–10). The α-PVDF bands at 974, 795, 764 and 614 cm^{-1} can be clearly observed in pure PVDF [29]. However, these bands disappear completely in the samples containing organoclays (Figs. 8–10). Simultaneously, strong β-PVDF bands are observed at 839 and 510 cm^{-1}, indicating a change in the crystalline morphology. PVDF with unmodified clay exhibits predominantly α-phase in spite of forming an intercalated nanocomposite. However, there is a small fraction of the β-phase in the nanocomposites, as evidenced from the weak absorption band at 840 cm^{-1} in the case of PVDF5CNa in Fig. 7.

The fraction of β-phase, $F(\beta)$, calculated from FTIR spectra, is presented in Table 4, assuming that there is no absorbance contribution from the clay. The β-phase fraction increases with clay concentration in all the cases. It is interesting to note that by adding only 0.5 wt% of organoclay (C10A), around 90% β-PVDF is obtained. The different organoclays, currently used in this study, did not show much variation in the $F(\beta)$ values. However, upon addition of 5 wt% of phosphonium clay (C18P), the PVDF almost completely crystallizes into the β-phase. Unmodified clay produces up to 23% of β-phase with 5 wt% loading along with a predominant α-phase. The results indicate that the modified clay, C18P, is most efficient in forming the β-phase.

3.4. Crystallization

DSC heating and cooling curves are plotted in Figs. 11 and 12, respectively, and the corresponding data are presented in Table 5. From the data it is observed that the addition of clay (both

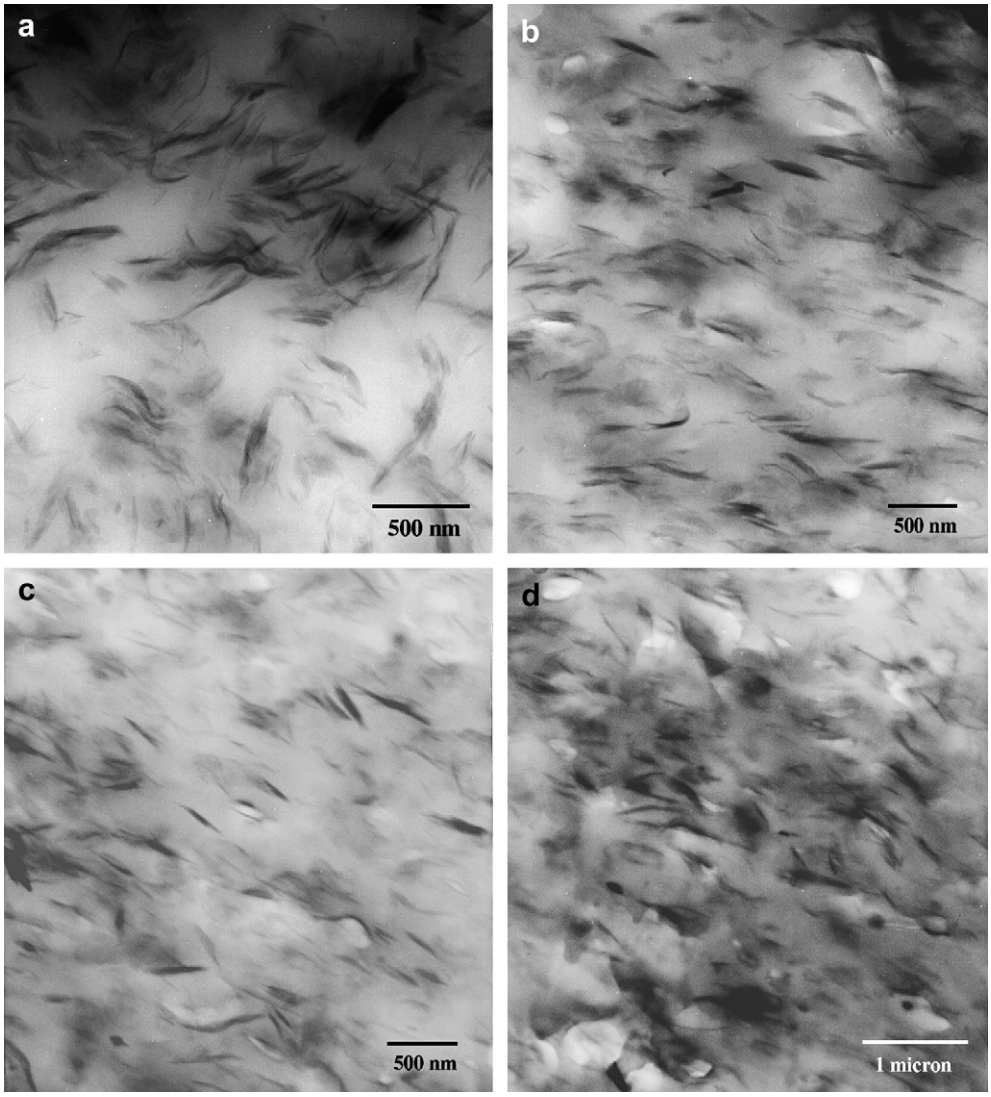

Fig. 4. Bright field TEM images of PVDF–clay nanocomposites with 2 wt% clay (a) C10A, (b) C18P, (c) CHDP and (d) C18P at lower magnification.

unmodified and organoclay) in PVDF results in the decrease in the enthalpy changes for crystallization and melting (ΔH_c and ΔH_m), implying a decrease in the crystallinity in PVDF. The decrease is higher in the case of organoclays. The percentage crystallinity (X_c) is calculated by dividing the heat of fusion for 100% crystalline PVDF to ΔH_m (1st heating) of sample. X_c decreases with clay concentration in the case of ammonium (C10A) and pyridinium (CHDP) clay nanocomposites. X_c also decreases with phosphonium clay (C18P) concentration, except in the case of 2 wt% C18P. The nanocomposites with 5 wt% of C18P show a doublet peak for both melting (Fig. 11) and crystallization (Fig. 12) events. Correspondingly, X_c is slightly higher compared to that of other organoclays with same amount of clay (5 wt%). This may be because of partially aggregated structures formed with 5 wt% C18P which could be observed in WAXD pattern of PVDF5C18P (Fig. 3c). CHDP has lower X_c values compared to PVDF and other clays as well. The decrease in crystallinity is most likely due to the interaction between the clay and PVDF, which appears to be quite strong as evidenced by the formation of the β-phase.

Table 3
Structure of PVDF nanocomposites having 5 wt% of different organoclays, determined from WAXD and TEM

Sample	$d_{(001)}$-Spacing of clay (Å)	$d_{(001)}$-Spacing of nanocomposites from WAXD (Å)	Average thickness of clay tactoids in nanocomposites (Å)
PVDF5CNa	12.4	13.1	–
PVDF5C10A	19.2	No peak	25
PVDF5C18P	19.6	19.6	35
PVDF5CHDP	17.5	No peak	23

The equilibrium melting temperature (T_m) and crystallization temperature (T_c) increased significantly upon addition of small amount of organoclay as given in Table 5. For example, PVDF with 5 wt% of C18P showed a maximum increase of 10 °C in T_m, whereas PVDF with unmodified clay (PVDF2CNa and PVDF5CNa) showed only a slight increase in T_m. The maximum increase in T_c (13 °C) is observed with 2 and 5 wt% of C18P. T_c also increased slightly with unmodified clay, but the increase was less than that for organoclay nanocomposites. The increase in melting and crystallization temperatures is related to the formation of β-phase as reported by Buckley et al. [17].

The cooling curves also give an indication of the rate of crystallization from the width of the crystallization peaks. The unmodified clay (CNa) results in faster crystallization as compared to PVDF, while the organoclays result in slightly slower crystallization.

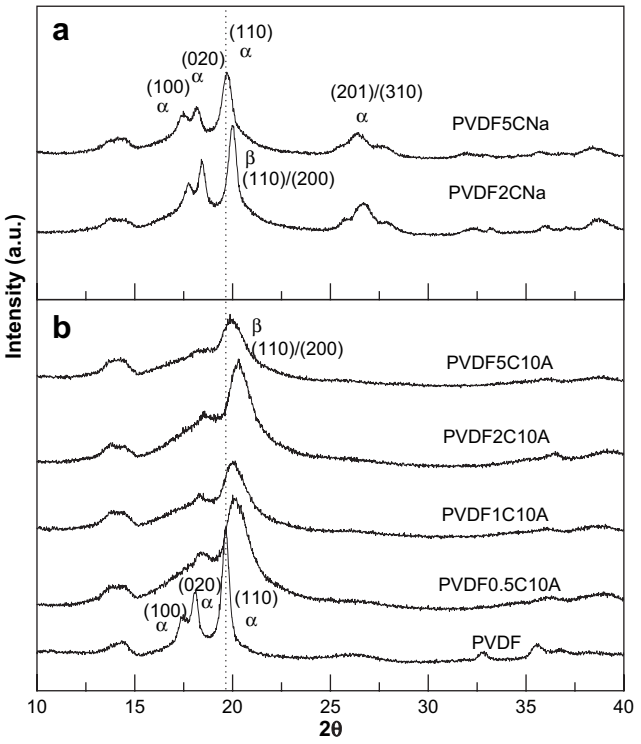

Fig. 5. WAXD patterns of (a) PVDF with CNa and (b) PVDF with C10A nanocomposites.

3.5. Small angle X-ray scattering studies

Lorentz's corrected intensity, $I(q)q^2$, vs. q is plotted in Figs. 13–16. The peaks obtained from the curves indicate that the periodicity of the crystalline lamella and the amorphous region is retained, while crystallizing from the melt, in the pure PVDF and nanocomposites

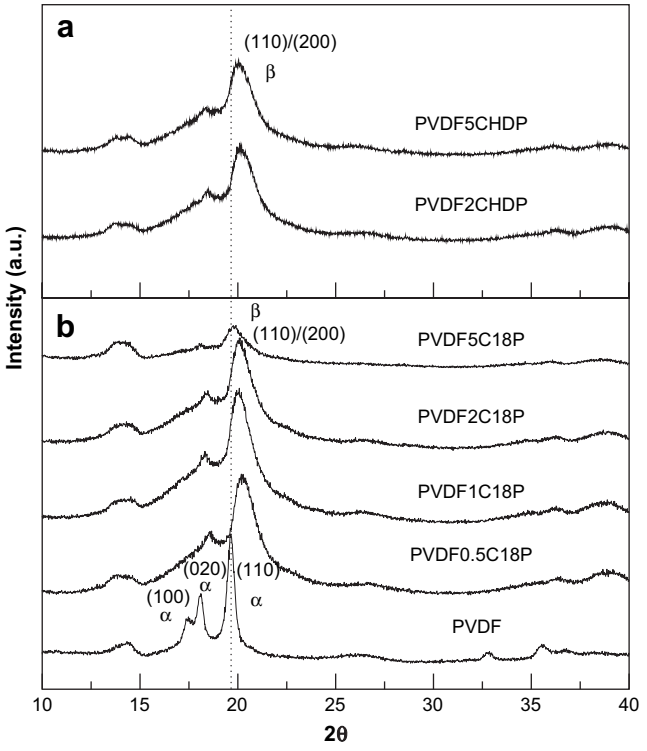

Fig. 6. WAXD patterns of (a) PVDF with CHDP and (b) PVDF with C18P nanocomposites.

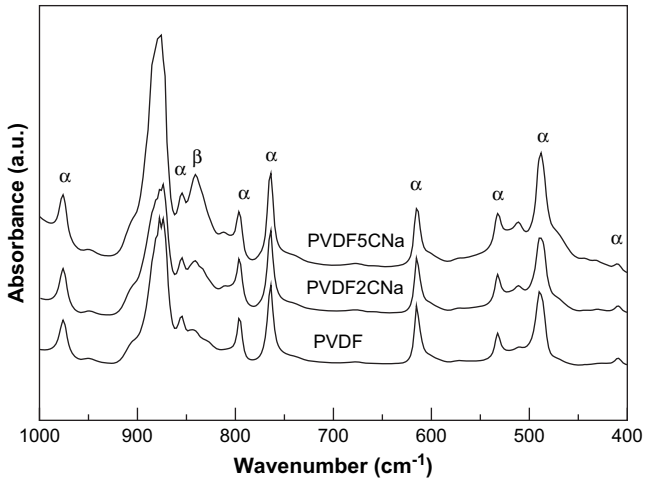

Fig. 7. FTIR spectra of PVDF with CNa nanocomposites.

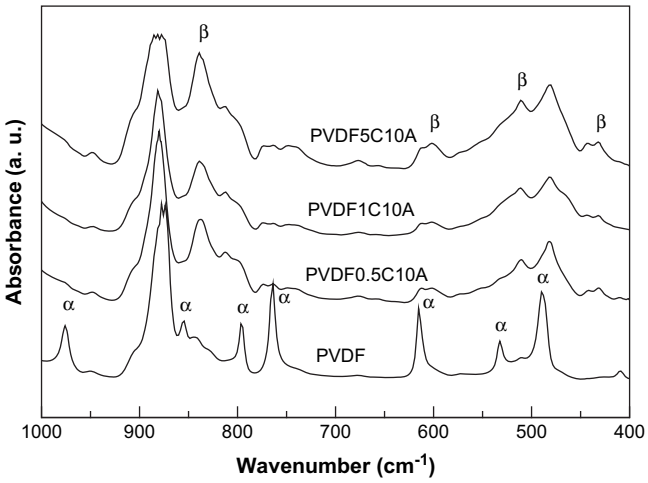

Fig. 8. FTIR spectra of PVDF with C10A clay nanocomposites.

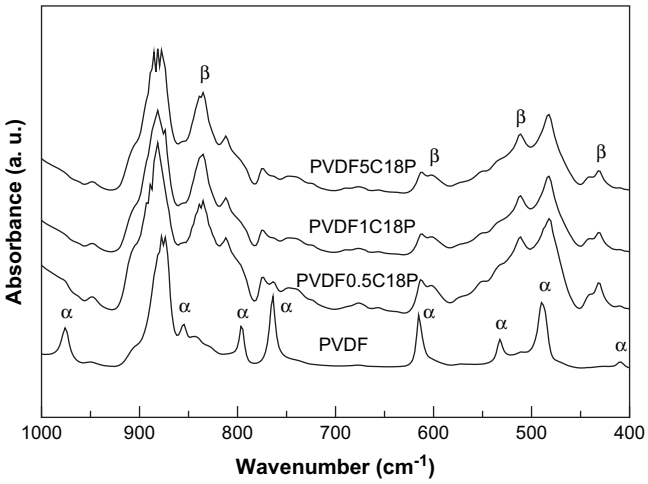

Fig. 9. FTIR spectra of PVDF with C18P nanocomposites.

as well. It is observed that the value of the scattering vector, q, at $I(q)q^2$ maxima is shifted slightly towards higher values of q on the addition of clay and is seen for all the clay concentrations. However, the shifting of the peak is less in the case of unmodified clay as compared to the organoclays. The scattering intensity decreases

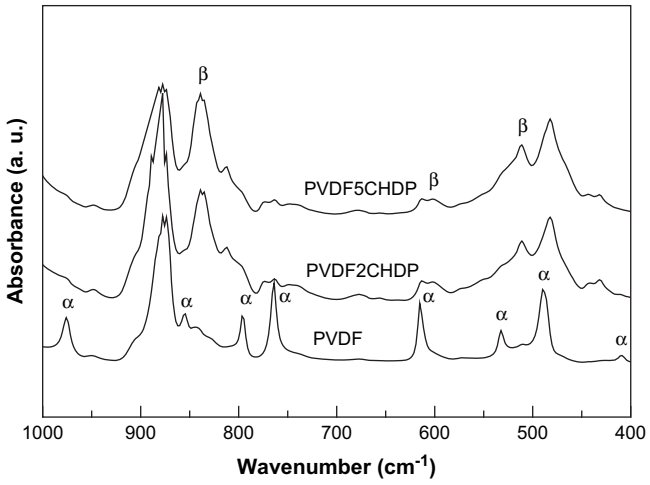

Fig. 10. FTIR spectra of PVDF with CHDP nanocomposites.

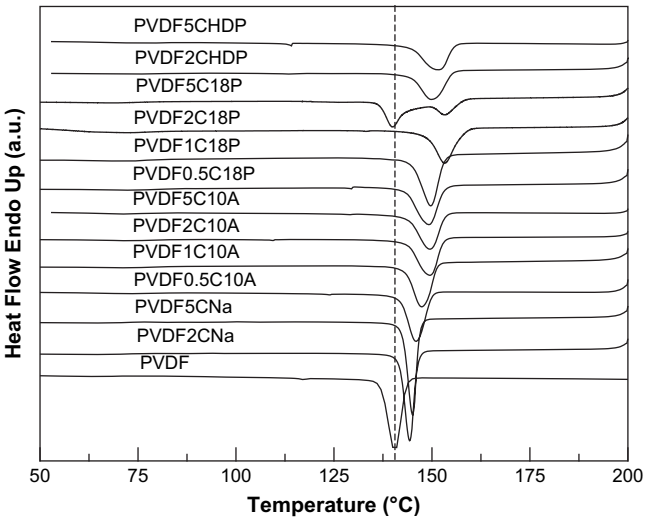

Fig. 12. DSC cooling curves of PVDF and PVDF–clay nanocomposites.

Table 4
Fraction of β-phase, $F(\beta)$, calculated from FTIR spectra, of PVDF and PVDF–clay nanocomposites

Sample	Clay content (%)	$F(\beta)$
PVDF	0	0.04 (±0.01)
PVDF2CNa	2	0.12 (±0.03)
PVDF5CNa	5	0.23 (±0.04)
PVDF0.5C10A	0.5	0.90 (±0.05)
PVDF1C10A	1	0.91 (±0.04)
PVDF2C10A	2	0.95 (±0.02)
PVDF5C10A	5	0.96 (±0.02)
PVDF0.5C18P	0.5	0.86 (±0.04)
PVDF1C18P	1	0.96 (±0.03)
PVDF2C18P	2	0.98 (±0.02)
PVDF5C18P	5	0.99 (±0.03)
PVDF2CHDP	2	0.90 (±0.04)
PVDF5CHDP	5	0.93 (±0.02)

Table 5
DSC parameters of PVDF and PVDF–clay nanocomposites

Sample	ΔH_m (J/g)		ΔH_c (J/g)	T_m (°C)	T_c (°C)	X_c (%)
	1st Heating	2nd Heating				
PVDF	68.1	66.5	59.4	165.6	140.3	66.3
PVDF2CNa	60.8	60.2	50.0	167.0	144.3	59.2
PVDF5CNa	65.7	60.2	51.9	167.1	145.1	64.0
PVDF0.5C10A	67.4	60.8	49.6	173.5	145.9	65.6
PVDF1C10A	56.4	48.3	44.8	173.5	147.4	54.9
PVDF2C10A	54.7	55.6	43.2	174.2	149.5	53.3
PVDF5C10A	53.0	40.7	40.1	174.0	149.5	51.6
PVDF0.5C18P	67.5	54.4	45.2	174.3	149.2	65.7
PVDF1C18P	55.2	57.9	50.8	174.7	149.7	53.7
PVDF2C18P	66.1	58.8	41.6	175.6	153.3	64.4
PVDF5C18P	54.4	58.8	49.3	175.5	153.4	53.0
PVDF2CHDP	53.5	51.9	36.5	174.8	150.0	52.1
PVDF5CHDP	52.0	42.4	37.1	174.4	151.6	50.6

The measurements were done on as-extruded nanocomposite samples.

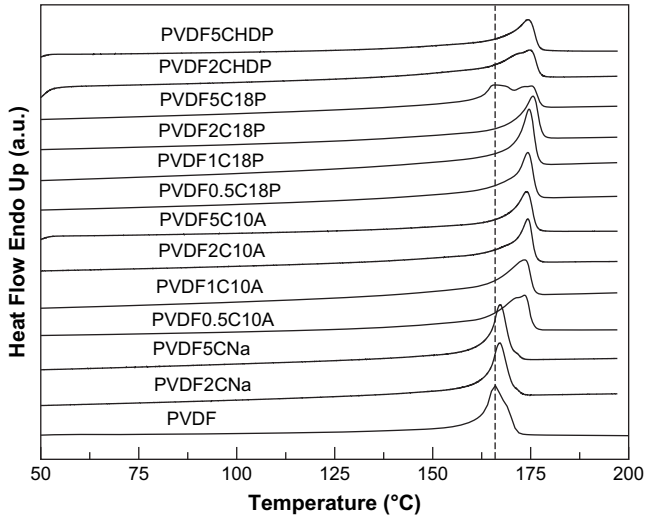

Fig. 11. DSC heating curves of PVDF and PVDF–clay nanocomposites.

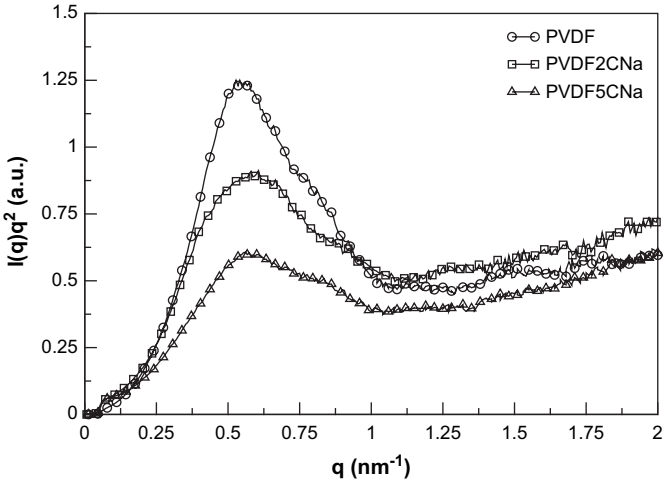

Fig. 13. Lorentz's corrected intensity, $I(q)q^2$, vs. q plots of PVDF and PVDF–CNa nanocomposites.

consistently with the clay percentage and the peaks become broader in all the cases. The broadening of the SAXS peak is due to the formation of the β-phase PVDF [17].

The long period, L_w, crystalline lamellar thickness, L_c, and the thickness of amorphous region, L_a, calculated using the q corresponding to the maximum of the curves are presented in Table 6. The long period, L_w, which is the sum of the average thicknesses of the crystalline lamella and the amorphous region ($L_c + L_a$) [32], decreases consistently with increasing the clay content. The long period for pure PVDF is 116.3 Å and it decreases to 92.9 Å for

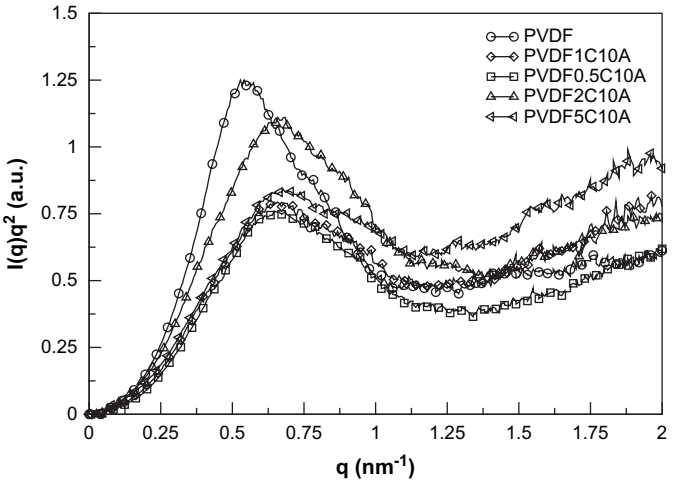

Fig. 14. Lorentz's corrected intensity, $I(q)q^2$, vs. q plots of PVDF and PVDF–C10A nanocomposites.

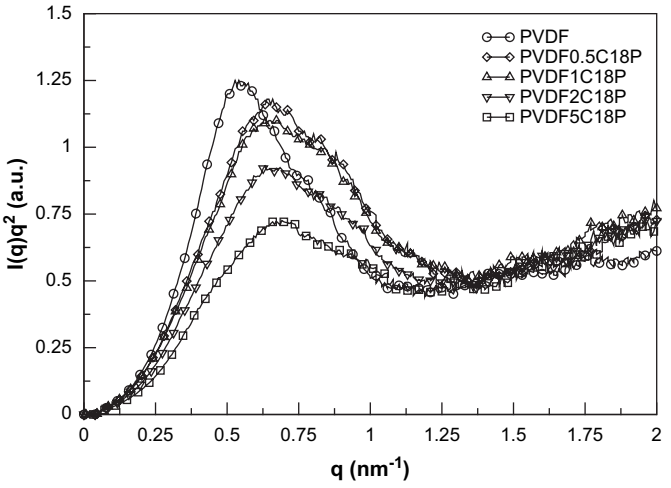

Fig. 15. Lorentz's corrected intensity, $I(q)q^2$, vs. q plots of PVDF and PVDF–C18P nanocomposites.

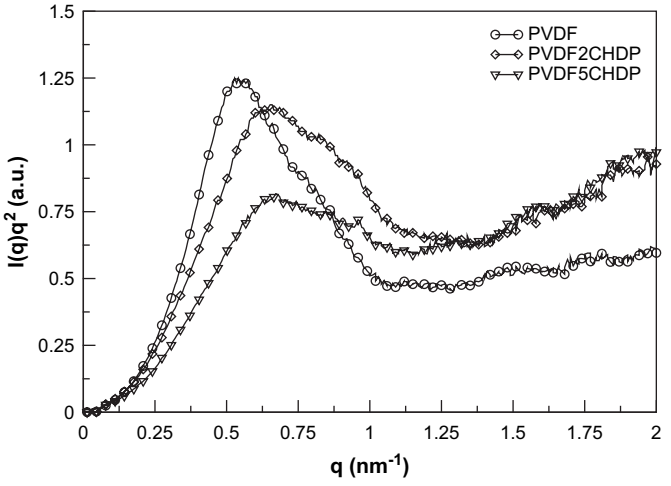

Fig. 16. Lorentz's corrected intensity, $I(q)q^2$, vs. q plots of PVDF and PVDF–CHDP nanocomposites.

PVDF5C10A. The crystalline lamella thickness decreases and the thickness of amorphous region increases with the addition of clay. L_W is found to be lowest (90.6 Å) with 5 wt% of C18P; however, the X_c for this nanocomposite is relatively higher than other clays with same clay concentration (Table 5), resulting in L_c values that are close to the other nanocomposites with organoclay (5 wt%). This indicates that C18P might form a larger number of smaller crystallites as compared to other clays. This phenomenon is further discussed in Section 3.6 which describes measurements of the average spherulitic size using SALS technique. Addition of unmodified clay also decreases the L_W. However, the decrease is smaller than that with organoclays. CHDP has low values of L_c as the crystallinity for these nanocomposites is lower compared to other clays.

Table 6
SAXS parameters determined from Lorentz's corrected intensity, $I(q)q^2$, vs. q curves

Sample	$L_W = 2\pi/q$ at I_{max} (Å)	L_c (Å)	L_a (Å)
PVDF	116.3	77.1	39.2
PVDF2CNa	106.7	63.2	43.5
PVDF5CNa	109.8	70.2	39.6
PVDF0.5C10A	96.3	63.2	33.1
PVDF1C10A	96.6	53.1	43.5
PVDF2C10A	94.3	50.2	44.1
PVDF5C10A	92.9	47.9	45.0
PVDF0.5C18P	97.7	64.2	33.5
PVDF1C18P	98.8	53.1	45.7
PVDF2C18P	94.9	61.1	33.8
PVDF5C18P	90.6	48.0	42.6
PVDF2CHDP	97.2	50.6	46.6
PVDF5CHDP	93.3	47.2	46.1

3.6. Hot-stage polarized optical microscopic studies

Fig. 17(a)–(d) shows the micrographs of isothermally crystallized samples of PVDF, PVDF2CNa, PVDF5CNa and PVDF0.5C18P. All samples were crystallized at 156 °C. The spherulitic size decreases with content of unmodified clay, as shown in micrographs (Fig. 17(b) and (c)). However, very small spherulites are obtained on the addition of a small amount of organoclay (0.5 wt%). Similar results were also obtained for other organoclays. This indicates that modified clays act as efficient nucleating agents for PVDF crystallization. The nanocomposite samples were also crystallized at higher temperatures (163 and 170 °C), with the objective of obtaining bigger spherulites due to the lower degree of supercooling. All the samples containing organoclay again gave very small spherulites.

3.7. Spherulite size

Fig. 18 presents the images of SALS patterns obtained from small angle light scattering (SALS) measurements on PVDF ((a) and (b)) and nanocomposites ((c)–(f)). All the samples were isothermally crystallized at 156 °C except that in Fig. 18(b) which was prepared by compression molding at 200 °C. Four-lobe patterns, indicating spherulites, were obtained for PVDF and nanocomposites with unmodified clay at all compositions as shown in Fig. 18. In the case of organoclay nanocomposites using C10A and C18P, clear four-lobe patterns were obtained only at the lowest clay loadings studied. No patterns were observed for nanocomposites having higher concentrations of organoclays (1 wt% or above) due to the formation of very small spherulites at higher clay loadings. The four-lobe pattern for the compression-molded PVDF film is larger than the isothermally crystallized film implying smaller spherulites. This is expected due to the higher degree of supercooling during crystallization during compression molding.

Table 7 presents the average spherulitic radius of the PVDF films obtained from SALS using Eq. (2). The average spherulitic radius for compression-molded PVDF film is found to be 18.8 μm and it

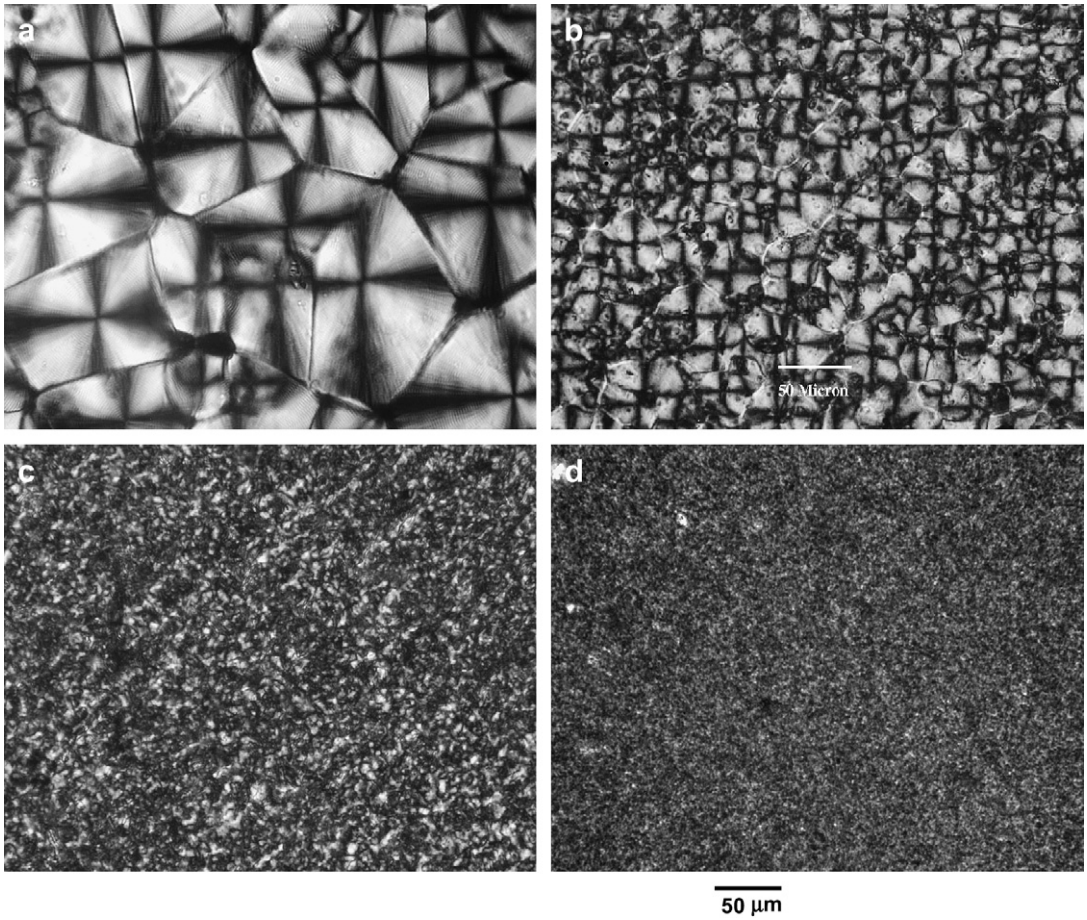

Fig. 17. Polarized optical micrographs of (a) PVDF, (b) PVDF2CNa, (c) PVDF5CNa and (d) PVDF0.5C18P at 20× resolution. All samples were isothermally crystallized at 156 °C, in a hot-stage until maximum size of spherulites is obtained.

increases to 22.8 μm when crystallized from melt at 156 °C. In the case of unmodified clays, the average spherulitic radius decreases from 22.8 μm for pure PVDF to 13.3 μm for 2 wt% CNa and 8.1 μm for 5 wt% CNa (Table 7). These results are in good agreement with the optical microscopic experiments discussed earlier. For organoclays, the average spherulitic radius reduced from 22.8 μm for pure PVDF to 9.7 μm for 0.5 wt% of C10A (ammonium clay) and 4.6 μm for 0.5 wt% of C18P (phosphonium clay) as given in Table 7. From the above observations, it can be concluded that the phosphonium based clay is a more efficient nucleating agent than the ammonium clay and the unmodified clay.

3.8. Mechanical properties

Table 8 presents the mechanical properties of PVDF and PVDF–clay nanocomposites. The tensile strength remains unaffected or increases slightly upon clay addition. However, the modulus decreases slightly in most of the cases except in the samples having phosphonium clays and 5 wt% of unmodified clay. The elongation at break increases significantly on the addition of ammonium (C10A) and pyridinium (CHDP) clays. The maximum increase is observed for 5 wt% of C10A (>200%). The next highest increase is shown by 5 wt% CHDP (around 175%). The addition of phosphonium clay (C18P) shows a relatively lower elongation, around 50% higher than pure PVDF. With 5 wt% of CNa, the elongation at break decreases to half that of the matrix polymer, whereas with 2 wt% of unmodified clay (CNa) the elongation at break increases by 70%.

The toughness of the polymer, defined as the area under the stress–strain curve, is also given in Table 8. Since the tensile strength does not vary much for the different nanocomposites the toughness varies in a manner similar to the elongation at break discussed above. At 5 wt% clay, the highest toughness is obtained for C10A followed by CHDP. The increase is around 170 and 150% higher than PVDF for C10A and CHDP, respectively. At 2 wt% clay, the toughness of C10A and CHDP is nearly the same (more than double of pure PVDF) followed by unmodified clay, CNa, which shows an increase of about 70%. Similar results have been published for PVDF [13,14] and other polymers with hectorite clay as well [33]. The enhanced toughness of PVDF–clay nanocomposites could be a combined effect of mobility of silicate layers in polymer matrix and the formation fiber-like β-phase in PVDF [13]. In addition, the formation of smaller spherulites in the presence of organoclay should also contribute to the enhanced toughness and elongation of nanocomposites. The differences in the elongation at break between the organoclays used may be due to the extent of dispersion obtained. The organoclays, C10A and CHDP, which are exfoliated (Fig. 3) have a higher elongation at break and toughness as compared to C18P, which is only partially exfoliated in PVDF matrix. The decrease in modulus is most likely due to decrease in crystallinity upon addition of clay.

Results of dynamic mechanical analysis carried out over a range of temperatures at a constant frequency of 1 Hz are shown in Fig. 19. It is clear from storage modulus (E') vs. temperature curves (Fig. 19(a)) that the storage modulus of all the nanocomposites except for PVDF5C18P is higher than pure PVDF throughout the temperature range from −100 to 150 °C. Ammonium clay (C10A) exhibits the highest storage modulus (E') over the temperature range compared to the other clays used. The addition of unmodified

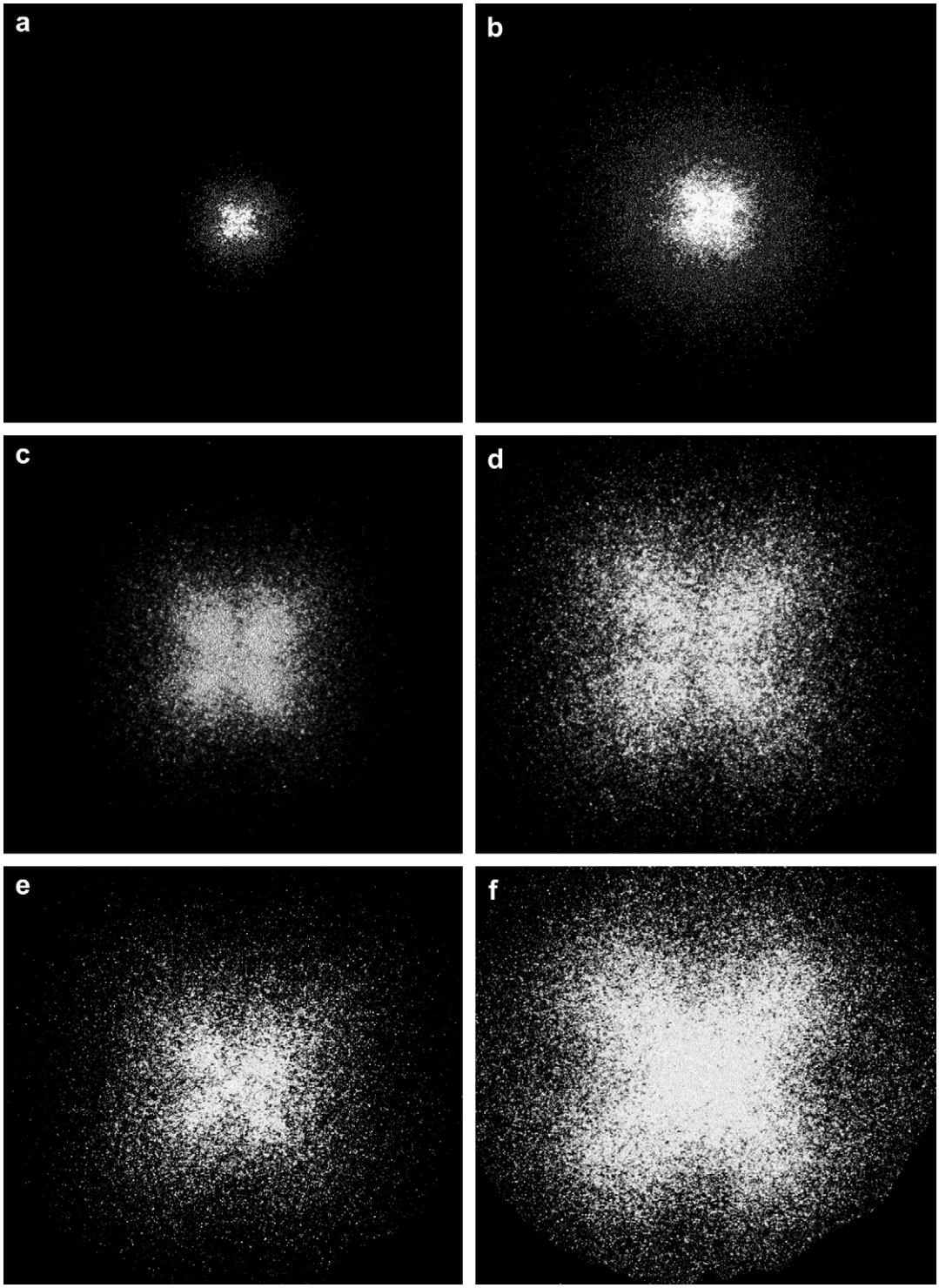

Fig. 18. Photographs of small angle light scattering (SALS) patterns of (a) isothermally crystallized PVDF, (b) PVDF film prepared under compression press at 200 °C and air-cooled, (c) and (d) 2 and 5 wt% unmodified clay (CNa), and (e) and (f) 0.5 wt% ammonium clay (C10A) and 0.5 wt% phosphonium clay (C18P), respectively. All samples except the sample shown in (b) were crystallized at 156 °C under hot-stage until the maximum size of spherulites is obtained and were used in small angle light scattering studies.

clay also increases the storage modulus significantly, although the improvement in tensile properties shown by the same clay is not considerable. Fig. 19(b) shows the loss modulus (E'') vs. temperature curves of PVDF and nanocomposites. The loss modulus (E'') increases with clay. There is a sharp decrease in E' and E'' above 100 °C for PVDF; however, this decrease is not seen for nanocomposites indicating an improved mechanical strength of nanocomposites at higher temperatures.

There are two thermal transitions observed in PVDF and its nanocomposites, as shown in Fig. 19(c). The transition at −34.5 °C, termed as β-relaxation, in the case of PVDF is ascribed to the micro-Brownian motions of chains in the amorphous regions, i.e., the glass transition temperature (T_g) [30,31]. The β-relaxation temperature does not change much with the addition of clay. The α-relaxation of PVDF, which is attributed to molecular motions in crystalline regions [34], was observed at around 115 °C, which is in agreement

Table 7
Average spherulitic radius of PVDF and PVDF–clay nanocomposites, calculated from small angle light scattering experiments

Sample	Average spherulitic radius, R (μm)
PVDF	22.8
PVDF-cm	18.8
PVDF2CNa	13.3
PVDF5CNa	8.1
PVDF0.5C10A	9.7
PVDF0.5C18P	4.6

All samples were crystallized from melt isothermally at 156 °C in a hot-stage except PVDF-cm which was made by compression molding at 200 °C followed by air-cooling.

with Lovinger and Wang [30]. The α-relaxation peak shifted towards higher temperature (around 130 °C) with organoclay, where the β-phase is prevalent. However, the peak shifted towards lower temperature to around 100 °C with 5 wt% of unmodified clay as shown in Fig. 19(b). There is another weak transition seen at around 57 °C in PVDF, termed as β′, which is due to the folding of the chains in the amorphous regions [34]. The peak is shifted to a slightly higher temperature (60 °C), which may be due to the higher fraction of amorphous content in nanocomposites as obtained from DSC (Table 6). The T_g, indicated by the peak in the tan δ vs. temperature curves, does not change much upon clay addition (Fig. 19(c)).

3.9. Dielectric constant measurements

Figs. 20 and 21 show the variation of permittivity and dielectric loss with frequency for the different nanocomposites. The data for the PVDF are also shown in the figures for comparison. Fig. 20 shows that there is an increase in dielectric constant values ranging from 2 to 8 units upon addition of clay, at 1 Hz frequency. The nanocomposites have a higher dielectric constant than pure PVDF throughout the frequency range, irrespective of the clay type. The dielectric constant values increase with clay content in all the cases. The dielectric loss also increases with clay for lower frequencies. However, it gradually decreases and remains almost comparable to the values for PVDF from a frequency range of 10^2 Hz to 1 MHz. PVDF has a dielectric constant of 8 at 1 Hz frequency; however, with the addition of 5 wt% unmodified clay, the dielectric constant increases to 13.3 at the same frequency. Since the PVDF has predominantly α-phase crystals, the increase in dielectric constant in this case may be because of the charge contribution from clay. As expected, the dielectric constant values for organoclay nanocomposites are found to be higher than the PVDF and PVDF with unmodified clay, the values are 14.8, 16.3 and 14.0 for PVDF5C10A, PVDF5C18P and PVDF5CHDP, respectively, at a frequency of 1 Hz. The increase in the dielectric constant accompanied by dielectric loss comparable to PVDF at higher frequencies could be attributed to the polarization obtained by the clay induced β-PVDF which has a higher charge storage capacity due to its polar nature [35] as well as from clay due to its charged surface.

Table 8
Mechanical properties of PVDF and PVDFC10A nanocomposites

Sample	Energy (area under the stress–strain curve) (J)	Tensile strength (MPa)	Tensile modulus (MPa)	Elongation at break (%)
PVDF	6.4 (±0.7)	45.2 (±0.4)	705 (±16.1)	117 (±13.5)
PVDF2CNa	10.8 (±0.6)	46.2 (±0.6)	674 (±18.8)	199 (±11.6)
PVDF5CNa	2.3 (±0.5)	46.8 (±0.4)	714 (±16.4)	42 (±8.4)
PVDF0.5C10A	6.6 (±0.8)	45.2 (±0.7)	689 (±13.8)	122 (±14.9)
PVDF1C10A	7.0 (±0.8)	45.4 (±0.7)	683 (±16.3)	128 (±15.0)
PVDF2C10A	13.8 (±0.8)	45.6 (±0.3)	668 (±18.6)	256 (±13.7)
PVDF5C10A	17.2 (±0.7)	46.1 (±0.2)	662 (±16.6)	317 (±12.2)
PVDF0.5C18P	6.7 (±0.6)	45.3 (±0.8)	705 (±14.6)	124 (±10.9)
PVDF1C18P	6.6 (±0.5)	45.4 (±0.3)	713 (±12.7)	122 (±9.4)
PVDF2C18P	8.4 (±0.4)	46.7 (±0.7)	716 (±15.3)	155 (±8.1)
PVDF5C18P	9.5 (±0.8)	47.6 (±0.2)	745 (±15.1)	176 (±15.0)
PVDF2CHDP	13.1 (±0.3)	45.7 (±0.7)	694 (±15.2)	241 (±5.7)
PVDF5CHDP	15.8 (±0.5)	46.7 (±0.7)	667 (±17.2)	292 (±9.7)

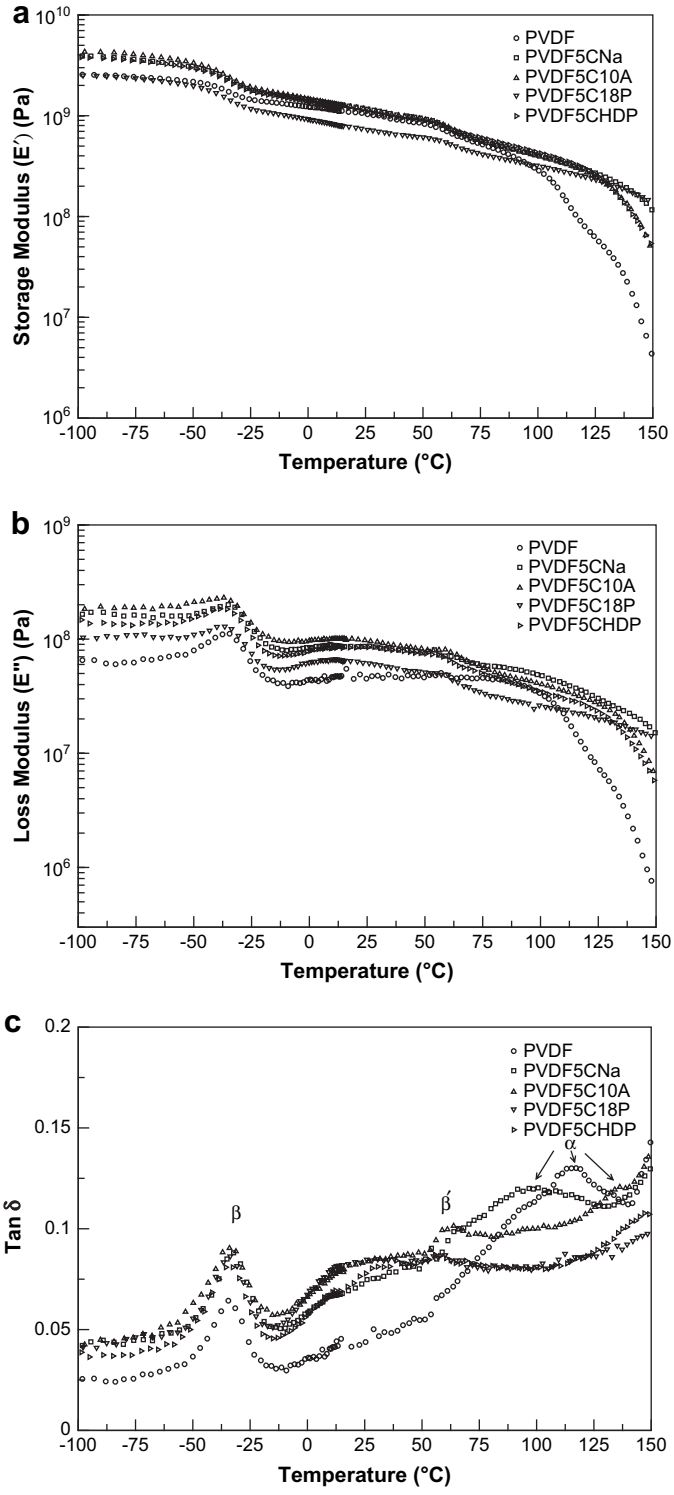

Fig. 19. Dynamic mechanical analysis of PVDF and PVDF–clay nanocomposites. (a) Storage modulus vs. temperature, (b) loss modulus vs. temperature and (c) tan δ vs. temperature curves.

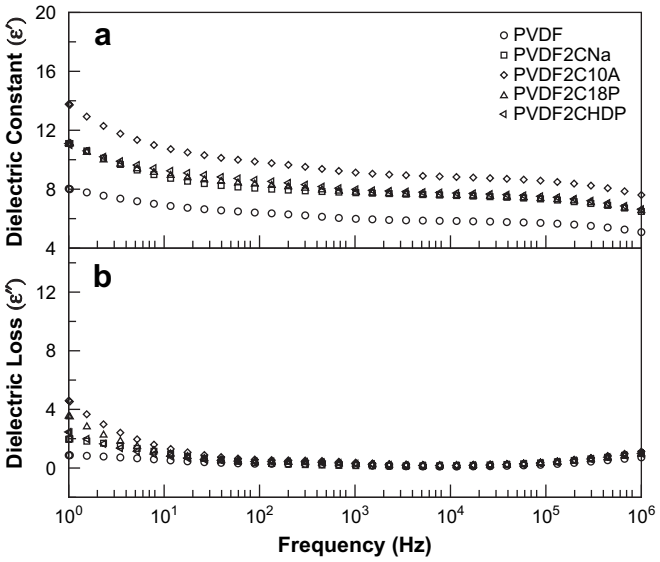

Fig. 20. (a) Relative dielectric constant and (b) dielectric loss of PVDF nanocomposites with 2 wt% of different clays.

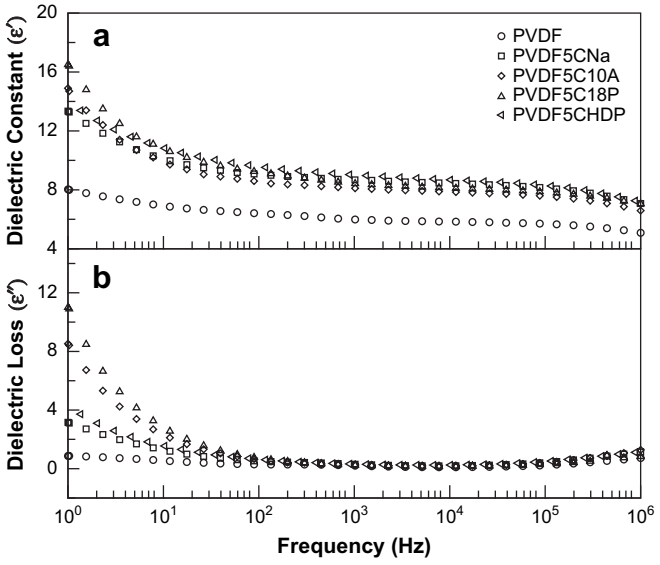

Fig. 21. (a) Relative dielectric constant and (b) dielectric loss of PVDF nanocomposites with 5 wt% of different clays.

4. Summary and conclusions

PVDF–clay nanocomposites were prepared by the melt-mixing process. Different organic surfactants were used to modify the montmorillonite clay. It was found from WAXD and TEM observations that the clay modified with different surfactants formed different nanocomposite structures. The ammonium and pyridinium surfactant modified clays gave nanocomposites with an exfoliated structure, whereas unmodified clay formed an intercalated nanocomposite structure. Phosphonium clay formed partially exfoliated nanocomposites.

Formation of β-PVDF was observed in the nanocomposites with all the organically modified clays, irrespective of their percentage, as evidenced from WAXD and FTIR studies. The fraction of β-phase increased with clay concentration and the highest fractions were obtained for the phosphonium surfactant modified clay. The addition of unmodified clay produced predominantly α-phase crystals and a small fraction of β-phase crystals, in spite of forming an intercalated nanocomposite structure.

SAXS studies showed that the long period (L_w) and crystalline lamellar thickness (L_c) decreased with clay concentration which is related to formation of the β-phase. DSC and hot-stage optical microscopy revealed a higher melting and crystallization temperatures and formation of smaller spherulites on addition of clay. The average spherulitic radius for isothermally crystallized samples, determined from SALS, decreased significantly (from 22.8 to 4.6 μm for C18P) on the addition of a small percentage (0.5 wt%) of organoclay. The phosphonium clay showed the highest increase in melting and crystallization temperatures and formed smaller spherulites compared to the other organic modifiers, and was found to be the most efficient nucleating agent. The percentage crystallinity (X_c) decreased significantly with clay. PVDF showed lower crystallinity in the presence of organoclay than unmodified clay. CHDP addition resulted in the lowest values of crystallinity.

Tensile measurements of PVDF nanocomposites indicated that the elongation at break and toughness increased significantly with two of organically modified clays and with the lower concentration of unmodified clay (2 wt%). The nanocomposites with ammonium modified clay showed the highest elongation at break (>200%) among the other organoclays and the unmodified clay. The phosphonium clay based nanocomposites had a significantly lower elongation at break compared to the other two organoclays. Tensile strength remained unaffected or increased slightly with addition of clay. However, the modulus decreased slightly in most of the cases except in the samples having phosphonium clay and a high percentage (5 wt%) of the unmodified clay. DMA showed a significant increase in the storage modulus. The glass transition temperature remained unchanged with the addition of clay. The dielectric constant increased with clay content, and the dielectric constant values were higher for organoclay nanocomposites as compared to the unmodified clay. Phosphonium clay showed the highest dielectric constant at frequency of 1 Hz.

The major conclusions of the work are:

- Phosphonium clay is more efficient in generating β-phase and is an effective nucleating agent for PVDF crystallization. It increases the melting and crystallization temperatures; and has the highest dielectric constant at lower frequencies among the nanocomposites studied.
- Ammonium clay has the best dispersion in PVDF matrix. It also improves the toughness of PVDF significantly.
- Pyridinium clay shows a good dispersion and improves the toughness of PVDF. It results in the lowest crystallinity among the nanocomposites.

The results presented indicate that both the chemical nature of the surfactant used to modify the clay and the extent of dispersion significantly affect the properties of the nanocomposites. Crystallization behaviour and electrical properties are most affected by the chemical nature of the clay while mechanical properties depend on both.

Acknowledgements

T.U.P. would like to thank the university grants commission (UGC), Govt. of India for providing his fellowship during the course of this work. The authors would like to thank Prof. Jayesh Bellare of Chem. Eng., IITB for providing SAXS facilities, Prof. Anil Kumar, Chemistry Dept., IITB for providing DSC facilities and Prof. A.R. Kulkarni, MEMS, IITB for dielectric experiments. Micro-compounding, Central Facility, IIT Bombay is thankfully acknowledged. The SAIF, IITB is acknowledged for providing TEM facilities.

References

[1] Lovinger AJ. Poly(vinylidene fluoride). In: Bassett E, editor. Developments in crystalline polymers – I. Applied Science Publishers/Cambridge University Press; 1982. p. 197–273.
[2] Salimi A, Yousefi AA. Polym Test 2003;22:699–704.
[3] Kawai H. Jpn J Appl Phys 1969;8:975–6.
[4] Fukada E, Furukawa T. Ultrasonics 1981;19:31–9.
[5] Lovinger AJ. Polymer 1981;22:412–3.
[6] Sajkiewicz P, Wasiak A, Goclowski Z. Eur Polym J 1999;35:423–9.
[7] Bergman Jr JG, McFee JH, Crane GR. Appl Phys Lett 1971;18:203–5.
[8] Miller R. J Polym Sci Polym Chem Ed 1976;14:2325.
[9] Wang J, Li H, Lui J, Duan Y, Jiang S, Yan S. J Am Chem Soc 2003;125:1496–7.
[10] Priya L, Jog J. J Polym Sci Part B Polym Phys 2002;40:1682–9.
[11] Priya L, Jog J. J Polym Sci Part B Polym Phys 2003;41:31–8.
[12] Priya L, Jog J. J Appl Polym Sci 2003;89:2036–40.
[13] Shah D, Maiti P, Gunn E, Schmidt D, Jiang DD, Batt CA, et al. Adv Mater 2004; 16(14):1173–7.
[14] Shah D, Maiti P, Jiang DD, Batt CA, Giannelis EP. Adv Mater 2005;17(5):525–8.
[15] Gersappe D. Phys Rev Lett 2002;89:058301-1–058301-4.
[16] Dillon DR, Tenneti KK, Li CY, Ko FK, Sics I, Hsiao BS. Polymer 2006;47:1678–88.
[17] Buckley J, Cebe P, Cherdark D, Crawford J, Ince BS, Jenkins M, et al. Polymer 2006;47:2411–22.
[18] Moussaif N, Groeninckx G. Polymer 2003;44:7899–906.
[19] Cebe P, Runt J. Polymer 2004;45:1923–32.
[20] Zhu J, Morgan AB, Lamelas FJ, Wilkie C. Chem Mater 2001;13:3774–80.
[21] Xiao J, Hu Y, Wang Z, Tang Y, Chen Z, Fan W. Eur Polym J 2005;41: 1030–5.
[22] Gregorio Jr R, Cestari M. J Polym Sci Part B Polym Phys 1994;32:859–70.
[23] Rosenberg Y, Siegmann A, Narkis M, Shkolnik S. J Appl Polym Sci 1991;43: 535–41.
[24] Misra A, Garg SN. J Polym Sci Part B Polym Phys 1986;24:999–1008.
[25] Vaia RA, Jandt KD, Kramer EJ, Giannelis EP. Macromolecules 1995;28: 8080–5.
[26] Yoon PJ, Hunter DL, Paul DR. Polymer 2003;44:5341–54.
[27] Giannelis EP, Krishnamoorti R, Manias E. Adv Polym Sci 1999;138:107–47.
[28] Wang Y, Cakmak M, White JL. J Appl Polym Sci 1985;30:2615–32.
[29] Lanceros-M'endez S, Mano JF, Costa AM, Schmidt VH. J Macromol Sci Phys 2001;B40:517–27.
[30] Lovinger AJ, Wang TT. Polymer 1979;20:725–32.
[31] Yano S. J Polym Sci Part A-2 1970;8:1057–72.
[32] Vonk CG. Synthetic polymers in the solid state. In: Glatter O, Kratky O, editors. Small angle X-ray scattering. Academic Press Inc.; 1982. p. 433–66.
[33] Haraguchi K, Ebato M, Takehisa T. Adv Mater 2006;18:2250–4.
[34] Mcbrierty VJ, Douglass DC, Weber TA. J Polym Sci Polym Phys Ed 1976;14: 1271–86.
[35] Newman BA, Scheinbeim JI, Yoon CH, Pae KD. Macromolecules 1983;16: 60–8.